ChemComm

COMMUNICATION

View Article Online
View Journal

Cite this: DOI: 10.1039/c5cc01659b

Received 25th February 2015,
Accepted 19th March 2015

DOI: 10.1039/c5cc01659b

www.rsc.org/chemcomm

Nanoporous silicon prepared through air-oxidation demagnesiation of Mg_2Si and properties of its lithium ion batteries†

Jianwen Liang, Xiaona Li, Zhiguo Hou, Cong Guo, Yongchun Zhu* and Yitai Qian*

Nanoporous silicon has been prepared through the air-oxidation demagnesiation of Mg_2Si at 600 °C for 10 hours ($Mg_2Si + O_2 \rightarrow Si + MgO$), followed by HCl washing. Mg_2Si was prepared from 200 mesh commercial Si at 500 °C for 5 h in an autoclave. The as-prepared Si exhibits a reversible capacity of 1000 mA h g^{-1} at 36 A g^{-1} and ~1200 mA h g^{-1} at 1.8 A g^{-1} over 400 cycles.

Silicon is a candidate anode material of lithium ion batteries (LIBs) owing to its high theoretical specific capacity of 3600 mA h g^{-1} and relatively low discharge potential (<0.5 V *versus* Li/Li^+).[1] However, Si exhibits rapid capacity fading over galvanostatic cycling caused by serious volume change (>300%) during lithiation–delithiation. Choosing nano-silicon or porous silicon materials as anodes is an effective strategy to address this issue.[2]

Various methods have been applied to prepare Si anode materials. Si anode materials can be synthesized from silica, such as magnesiothermic reduction,[3–6] electrochemical reduction in molten salts[7] and hydrothermal reduction with Mg.[8] Also, Si anode materials can be obtained by reduction of $SiCl_4$ in organic solvents[9,10] or in molten salts.[11]

Converting the commercial bulk Si powders into nano-Si or porous Si is an alternative route to obtain silicon anode materials of LIBs. Si nanoparticles obtained by high-energy ball-milling macro-sized Si particles displayed a performance of 1600 mA h g^{-1} at 240 mA g^{-1} after 600 cycles.[12] Porous Si/C composites were prepared based on the etching reaction of bulk Si and gas CH_3Cl with Cu-based catalyst assistance, which showed a discharge capacity of about 1036 mA h g^{-1} at 50 mA g^{-1} after 100 cycles.[13] Macroporous Si was produced *via* Ag deposition and chemical etching with HF and H_2O_2, after carbon coating, which showed a capacity of ~2200 mA h g^{-1} at 400 mA g^{-1} after 50 cycles.[14] Porous Si was synthesized through acid etching the Al–Si alloy (Al-80%, Si-20%) powder, which exhibited a discharge capacity of 281 mA h g^{-1} at 100 mA g^{-1} after 100 cycles.[15]

With regard to the conversion of Mg_2Si into Si, the previous work was carried out by metathesis reaction,[16–20] such as the reaction between Mg_2Si and $SiCl_4$ in organic solvents,[16] Mg_2Si reacted with amorphous silica or silicon monoxide through a high energy mechanical milling process.[21,22] Si nanoparticle anodes obtained by the reaction of Mg_2Si with $ZnCl_2$ ($Mg_2Si + ZnCl_2 \rightarrow MgCl_2 + Zn + Si$) showed a reversible capacity of 795 mA h g^{-1} at 3.6 A g^{-1} over 250 cycles. Recently, nanoporous silicon anodes synthesized through the reaction of Mg_2Si and molten bismuth (Bi) in high-purity He gas presented a capacity retention of 1500 mA h g^{-1} at 1.8 A g^{-1} after 500 cycles.[23]

In this study, we report the preparation of nanoporous silicon through air-oxidation demagnesiation of Mg_2Si at 600 °C for 10 h, following by HCl washing. Mg_2Si is prepared from 200 mesh commercial Si at 500 °C for 5 h in an autoclave. The as-obtained Si materials show a porous structure with a Brunauer–Emmett–Teller (BET) surface area of 86.6 m^2 g^{-1} and a pore size of ~4 nm. As an anode for rechargeable LIBs, nanoporous Si exhibits a reversible capacity of 1000 mA h g^{-1} at 36 A g^{-1} and ~1200 mA h g^{-1} at 1.8 A g^{-1} over 400 cycles. The related reaction in the air-oxidation demagnesiation of Mg_2Si can be expressed as follows: $Mg_2Si + O_2$ (air) $\rightarrow$ Si + MgO.

The XRD pattern of the sample after washing with HCl is shown in Fig. 1a, all the peaks can be indexed to cubic Si with a calculated lattice constant of a = 5.415 Å, close to the reported value of a = 5.430 Å (JPCDS 27-1402). Based on the Scherrer equation, the size of the Si particles is estimated to be about 15 nm. Scanning electron microscopy (SEM) images in Fig. 1b and Fig. S1 (ESI†) exhibit that the obtained Si sample appears as micrograins comprising of many nanoparticles. In the transmission electron microscopy (TEM) image of Fig. 1c, the disordered nanometer pores and nanoparticles of several nanometers can be clearly observed. The high-resolution transmission electron microscopy (HRTEM) image, shown in Fig. 1d, reveals lattice

Hefei National Laboratory for Physical Science at Micro-scale and Department of Chemistry, University of Science and Technology of China, Hefei, Anhui 230026, P. R. China. E-mail: ytqian@ustc.edu.cn, ychzhu@ustc.edu.cn

† Electronic supplementary information (ESI) available: Experimental details; SEM image and nitrogen adsorption curves of as-prepared silicon; characterization of previous commercial silicon, Mg_2Si/Mg and MgO/Si compounds during the experimental process; and table presenting several repeated experiments. See DOI: 10.1039/c5cc01659b

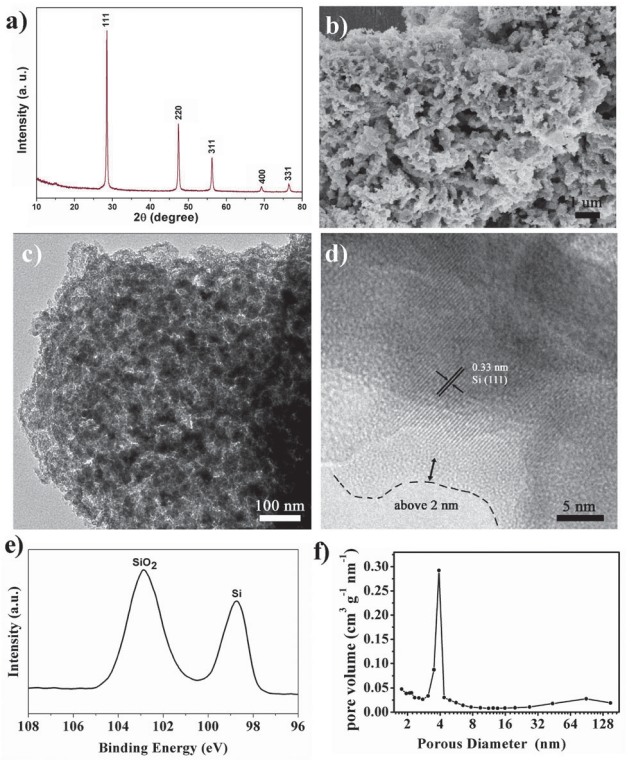

Fig. 1 (a) XRD pattern, (b) SEM image, (c) TEM image, (d) HRTEM image, (e) XPS spectrum, and (f) BJH pore diameter distribution of the as-prepared porous nano-Si.

fringes of the Si nanocrystals. The interplanar distances are measured to be about 0.33 nm, corresponding to the (111) crystal planes of the cubic Si. Besides, amorphous layers above 2 nm can be observed. The surface contents of the nanoporous Si are investigated using the Si 2p X-ray photoelectron spectroscopy (XPS) spectrum, as shown in Fig. 1e. A peak at ~103 eV indicates the existence of SiO_2.[24] The surface density of oxygen is further quantified to be as high as 61.2 at%, which is close to the theoretical content of pure SiO_2 (66.7 at%). The results of XPS and HRTEM give a hint that a small amount of amorphous SiO_2 is present on the surface of Si nanoparticles. Barrett–Joyner–Halenda (BJH, Fig. 1f) analysis of the nitrogen adsorption curves (Fig. S2, ESI†) indicates that the pore size of the Si sample is mainly ~4 nm. The BET surface area of the porous Si is 86.6 $m^2\ g^{-1}$.

Since the oxidized behaviors of magnesium and silicon are different, it is possible to control the oxidation process of Mg_2Si to obtain Si. For this purpose, we prepared Mg_2Si containing a small excess of Mg. A small excess of Mg should be helpful for the air-oxidation of Mg_2Si to Si at relatively lower temperatures. Using commercial silicon (200 mesh, SEM images in Fig. S3, ESI†) and metallic Mg with a Mg/Si ratio of 2.1, Mg_2Si with Mg in excess of 5 at% (Mg_2Si/Mg) was prepared at 500 °C for 5 h in an autoclave. The XRD pattern of the as-prepared Mg_2Si (Fig. 2a) confirms that the bulk Si converted to Mg_2Si (labeled as "■" JCPDS No. 35-0773) and the excess of Mg existing (labeled as "▲" JCPDS No. 04-0770). The SEM image of the Mg_2Si/Mg powder is shown in Fig. S4 (ESI†).

To find the appropriate temperature for the oxidation of Mg_2Si to Si, a series of related experiments concerning the

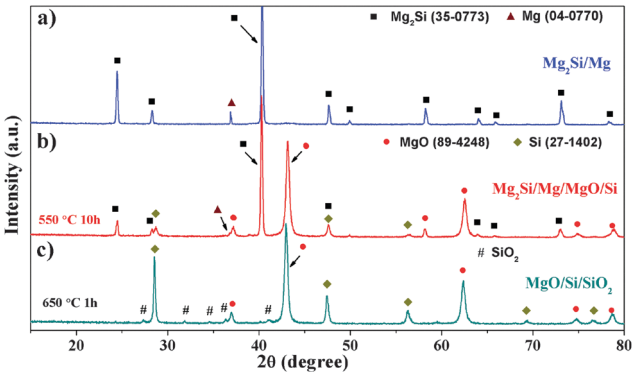

Fig. 2 XRD patterns of (a) Mg_2Si/Mg powder, and the as-prepared samples after the air-oxidation process at (b) 550 °C for 10 h, (c) 650 °C for 1 h.

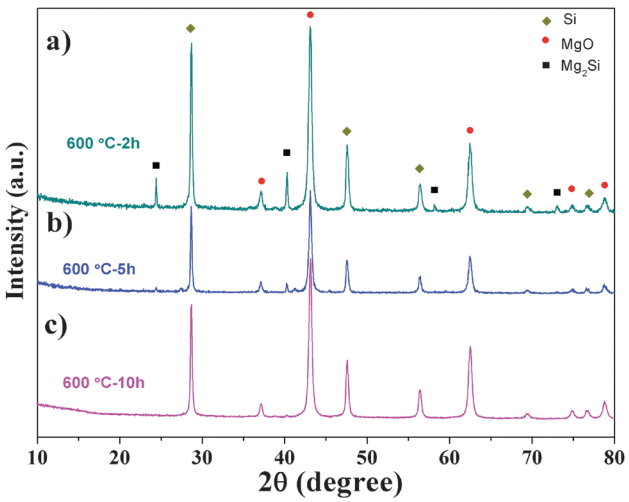

Fig. 3 XRD patterns of the raw product during oxidizing Mg_2Si/Mg in air at temperatures of 600 °C for (a) 2 h, (b) 5 h, (c) 10 h.

heating of as-prepared Mg_2Si/Mg in air was carried out at temperatures of 400 °C, 550 °C and 650 °C. When Mg_2Si/Mg was heated at 400 °C, the XRD pattern of the resulting products shows that there are only Mg_2Si and Mg (Fig. S5, ESI†) even after 10 h. As the temperature was increased to 550 °C, at 10 h, crystalline Si and MgO appear, however Mg_2Si remained (Fig. 2b). As the temperature was kept at 650 °C for 1 h, it is found that SiO_x (labeled as "#", JCPDS No. 81-0066, Fig. 2c) is observed in the products. So we set the temperature of air-oxidation of as-prepared Mg_2Si/Mg at 600 °C for 2 h, 5 h and 10 h. Fig. 3 shows the XRD patterns of the products obtained at 600 °C for 2 h, 5 h and 10 h, indicating that Mg_2Si can be completely transformed to Si after 10 h. The raw product of oxidizing Mg_2Si/Mg in air at 600 °C after 10 h is presented in Fig. 3c (the SEM image of the raw product is shown in Fig. S6, ESI†). The diffraction peaks (labeled as "◆") are characterized as 111, 220, 311, 400, and 331 planes of cubic Si (JCPDS No. 27-1402) and the peaks (labeled as "●" JCPDS No. 45-0946) are indexed to 111, 200, 220, 311 and 222 planes of MgO. The related reaction in the air-oxidation demagnesiation of Mg_2Si can be expressed as: $Mg_2Si + O_2$ (air) → $Si + 2MgO$. After washing with HCl, nanoporous Si can be obtained.

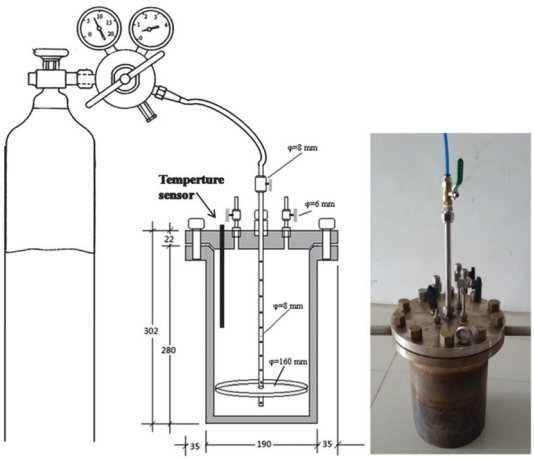

Fig. 4 The scheme and photo of the 5 L stainless steel reactor.

The air-oxidation demagnesiation of Mg_2Si was performed using a 5 L stainless steel reactor (Fig. 4). The as-prepared Mg_2Si/Mg was oxidized at a heating rate of 2 °C min^{-1} to 600 °C and then kept for 10 h under air flow. The final nano-silicon production is over 10 g for each experiment, and the yield of nano-silicon is above 90%. At the same time, the tap density of the nano-porous Si powder is estimated to be ~0.597 g cm^{-3}. The yields and the tap density of this nano-silicon material are calculated based on five repeated experiments which are provided in the ESI† (Table S1).

Next, the electrochemical performance of the nanoporous silicon anodes was investigated in CR2016 coin cells with lithium foil as a counter electrode. Fig. 5a shows the typical voltage profiles for the first five cycles of the as-synthesized Si electrode at a current density of 360 mA g^{-1}. In the first discharge curve, a plateau at around 0.8 V is assigned to the formation of a solid electrolyte interface (SEI) layer, which can result in an initial irreversible capacity loss and disappears in the subsequent cycles.[25] The discharge plateau located at around 0.2 V is related to the alloy formation process between Li and crystal Si. Subsequent discharge and charge cycle curves exhibit the voltage profiles characteristic of amorphous Si.[25–27] The porous Si electrode shows a discharge capacity of 3740 mA h g^{-1} and a charge capacity of 3291 mA h g^{-1} for the first cycle, corresponding to the initial Coulombic efficiency (CE) of 88%. Meanwhile, after cycling up to 85 cycles, the discharge capacity of the Si electrode is still retained at 2156 mA h g^{-1}, which is about 64% of its initial reversible capacity (Fig. 5b). Furthermore, the CE remains at about 100% after the first cycle, showing a good reversibility. While, a contrast electrode with the initial commercial bulk Si as an active material shows poor cycling stability, which is nearly reduced to 10 mA h g^{-1} at 15 cycles, thus further indicating that the good cycling performance of the as-prepared porous silicon electrode arises from the fabrication process.

The rate capability for the porous Si anode is evaluated using galvanostatic charge–discharge measurements upon increasing the current density from 0.36 A g^{-1} to 36 A g^{-1} and then back to 0.36 A g^{-1} (shown in Fig. 5c and d). It is obvious that the nanoporous silicon electrode exhibits reversible capacities of

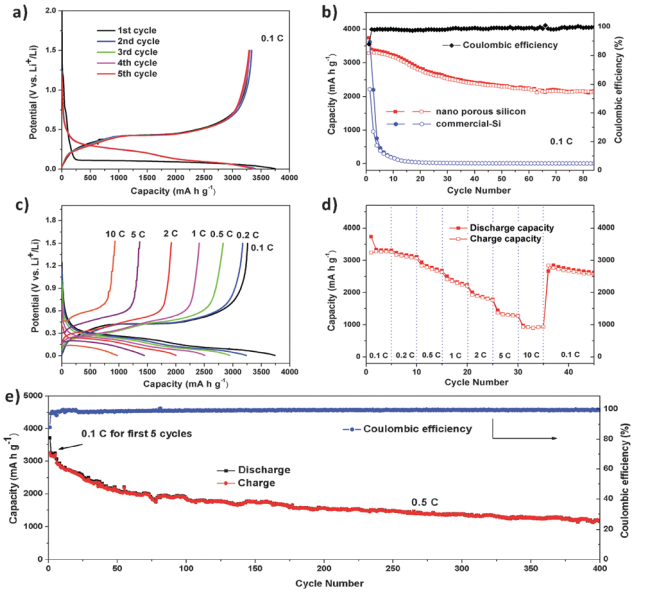

Fig. 5 Electrochemical performances of nanoporous silicon anodes. (a) Typical galvanostatic discharge–charge curves for the first five cycles of the nanoporous silicon sample in the potential region of 0.005–1.50 V *versus* Li/Li^+ at 360 mA g^{-1}. (b) Cycling properties of the cell with the nanoporous silicon and commercial bulk silicon sample at 360 mA g^{-1}. The solid symbol represents discharge capacity and the hollow symbol represents charge capacity. (c) The typical galvanostatic discharge–charge curves at different current densities, and (d) the rate performance of the nanoporous silicon sample and (e) long term cycling properties of the nanoporous silicon electrode at 1.8 A g^{-1}.

3335, 3187, 2941, 2508, 2003 and 1446 mA h g^{-1}, and the CE is almost 100% at current densities of 0.36, 0.72, 1.8, 3.6, 7.2 and 18 A g^{-1}, respectively. Even at a higher current density of 36 A g^{-1}, the electrode is able to maintain a capacity of ~1000 mA h g^{-1}. Moreover, the capacity could recover to approximately 2850 mA h g^{-1} when the current density goes back to 0.36 A g^{-1}. In addition, long cycling performance at a rate of 1.8 A g^{-1} was also tested. Gradual capacity fading in the initial cycles is observed for such high rate cycling, which is probably due to the lower electrical conductivity of the amorphous SiO_2 layer and the Si materials. In order to further improve the electrochemical performance, several strategies such as carbon coating, graphene encapsulation and preparation of high electrical conductivity metal composites can be adopted. After the initial dozens of cycles, the capacity in the 50th cycle is ~2100 mA h g^{-1} and remained stable at ~1200 mA h g^{-1} up to 400 cycles (57% capacity retention compared to the 50th cycle). These results indicate that both the porous structure and the surface coating of the amorphous SiO_2 layer play an important role in electrochemical performance of silicon anodes in LIBs. The nanostructure offers a short Li^+ diffusion path and large BET surface area just as the as-synthesized nanoporous silicon, which increased the number of active sites and enhanced the contact surface between the electrode material and the electrolyte.[4,28] Besides, the amorphous SiO_2 layer can protect nanoporous silicon material particles from the side reaction with the electrolyte.[29,30] Moreover, the existence of pores may effectively accommodate the

volume change of silicon and allow for facile strain relaxation without strong mechanical stress during cycling.[2]

In summary, we developed an air-oxidation demagnesiation of Mg_2Si to obtain nanoporous Si. As an anode for rechargeable lithium ion batteries, the as-prepared nanoporous Si exhibits high reversible capability, long-term cycling stability, high initial columbic efficiency and good rate performance. Each experiment can produce 10 g nanoporous silicon powder, and the yield is about 90%. Since Mg_2Si was prepared from 200 mesh commercial Si, compared with previous work, the route is relatively simple and suitable for the large scale production of Si nanomaterials.

This work was financially supported by the 973 Project of China (No. 2011CB935901) and the National Natural Science Fund of China (No. 21471142, 21201158).

Notes and references

1 M. Obrovac and V. Chevrier, *Chem. Rev.*, 2014, **114**, 11444–11502.
2 H. Wu and Y. Cui, *Nano Today*, 2012, **7**, 414–429.
3 J. Liang, D. Wei, N. Lin, Y. Zhu, X. Li, J. Zhang, L. Fan and Y. Qian, *Chem. Commun.*, 2014, **50**, 6856–6859.
4 H. Jia, P. Gao, J. Yang, J. Wang, Y. Nuli and Z. Yang, *Adv. Energy Mater.*, 2011, **1**, 1036–1039.
5 Z. Bao, M. Weatherspoon, S. Shian, Y. Cai, P. Graham, S. Allan, G. Ahmad, M. Dickerson, B. Church, Z. Kang, H. Abernathy, C. Summers, M. Liu and K. Sandhage, *Nature*, 2007, **446**, 172–175.
6 J. Liang, X. Li, Q. Cheng, Z. Hou, L. Fan, Y. Zhu and Y. Qian, *Nanoscale*, 2015, **7**, 3440–3444.
7 X. Jin, P. Gao, D. Wang, X. Hu and G. Chen, *Angew. Chem.*, 2004, **116**, 751–754.
8 J. Liang, X. Li, Y. Zhu, C. Guo and Y. Qian, *Nano Res.*, 2015, DOI: 10.1007/s12274-014-0633-6.
9 H. Kim, M. Seo, M. Park and J. Cho, *Angew. Chem., Int. Ed.*, 2010, **49**, 2146–2149.
10 J. Heath, *Science*, 1992, **258**, 1131–1133.
11 N. Lin, Y. Han, L. Wang, J. Zhou, J. Zhou, Y. Zhu and Y. Qian, *Angew. Chem., Int. Ed.*, 2015, **54**, 3822–3825.
12 M. Gauthier, D. Mazouzi, D. Reyter, B. Lestriez, P. Moreau, D. Guyomard and L. Roue, *Energy Environ. Sci.*, 2013, **6**, 2145–2155.
13 Z. Zhang, Y. Wang, W. Ren, Q. Tan, Y. Chen, H. Li, Z. Zhong and F. Su, *Angew. Chem., Int. Ed.*, 2014, **53**, 5165–5169.
14 B. Bang, J. Lee, H. Kim, J. Cho and S. Park, *Adv. Energy Mater.*, 2012, **2**, 878–883.
15 Z. Jiang, C. Li, S. Hao, K. Zhu and P. Zhang, *Electrochim. Acta*, 2014, **115**, 393–398.
16 C. Yang, R. Bley, S. Kauzlarich, H. Lee and G. Delgado, *J. Am. Chem. Soc.*, 1999, **121**, 5191–5195.
17 L. Wang, N. Lin, J. Zhou, Y. Zhu and Y. Qian, *Chem. Commun.*, 2015, **51**, 2345–2348.
18 D. Neiner, H. Chiu and S. Kauzlarich, *J. Am. Chem. Soc.*, 2006, **128**, 11016–11017.
19 K. Pettigrew, Q. Liu, P. Power and S. Kauzlarich, *Chem. Mater.*, 2003, **15**, 4005–4011.
20 Y. Hwa, W. Kim, B. Yu, J. Kim, S. Hong and H. Sohn, *J. Power Sources*, 2014, **252**, 144–149.
21 P. McMillan, J. Gryko, C. Bull, R. Arledge, A. Kenyon and B. Cressey, *J. Solid State Chem.*, 2005, **178**, 937–949.
22 R. Epur, L. Minardi, M. Datta, S. Chung and P. Kumta, *J. Solid State Chem.*, 2013, **208**, 93–98.
23 T. Wada, T. Ichitsubo, K. Yubuta, H. Segawa, H. Yoshida and H. Kato, *Nano Lett.*, 2014, **14**, 4505–4510.
24 M. Alexander, R. Short, F. Jones, W. Michaeli and C. Blomfield, *Appl. Surf. Sci.*, 1999, **137**, 179–183.
25 J. Maranchi, A. Hepp and P. Kumta, *Electrochem. Solid-State Lett.*, 2003, **6**, A198–A201.
26 J. Li and J. Dahn, *J. Electrochem. Soc.*, 2007, **154**, A156–A161.
27 T. Hatchard and J. Dahn, *J. Electrochem. Soc.*, 2004, **151**, A838–A842.
28 M. T. McDowell, I. Ryu, S. Lee, W. C. Wang, W. D. Nix and Y. Cui, *Adv. Mater.*, 2012, **24**, 6034–6041.
29 H. Wu, G. Chan, J. W. Choi, I. Ryu, Y. Yao, M. T. McDowell, S. Lee, A. Jackson, Y. Yang, L. Hu and Y. Cui, *Nat. Nanotechnol.*, 2012, **7**, 310–315.
30 S. Sim, P. Oh, S. Park and J. Cho, *Adv. Mater.*, 2013, **25**, 4498–4503.

